

Article

Biomechanical Study of Proximal Femur for Designing Stems for Total Hip Replacement

William Solórzano ^{1,*} , Carlos Ojeda ¹ and Andres Diaz Lantada ^{2,*}

¹ Mechanical Technology Laboratory, Department of Mechanical and Electrical Engineering, Universidad de Piura, Piura 20009, Peru; carlos.ojeda@udep.edu.pe

² Product Development Laboratory, Department of Mechanical Engineering, Universidad Politécnica de Madrid, c/ José Gutiérrez Abascal 2, 28006 Madrid, Spain

* Correspondence: wsrequejo@gmail.com or william.solorzano@alum.udep.edu.pe (W.S.); adiaz@etsii.upm.es (A.D.L.); Tel.: +51-94-325-7910 (W.S.)

Received: 26 March 2020; Accepted: 16 June 2020; Published: 19 June 2020



Abstract: Innovative hip implants should be designed in accordance with biomechanical models of the proximal femur and take into account both body weight and muscle action in order to improve usability and biomimetic performance. This article proposes a finite element analysis of the proximal femur using both cortical and trabecular regions and employing transverse isotropic properties with standardized loads taken from active and young patients. Maximum principal stresses are plotted to show the mechanical behavior of the femur and grouped to evaluate stress shielding. Tsai–Wu and the maximum principal stress fields are useful for finding the areas more prone to failure and analyzing the influence of the stems on femoral mechanics. Other parameters, such as the stem material, absence of neck and osteotomy level, are explained. This paper is expected to provide a guide for designers and surgeons of femoral stems for assessing qualitatively and quantitatively the risks of stress shielding.

Keywords: proximal femur; biomechanics; finite element analysis; stress shielding; hip replacement

1. Introduction

Bone is a dynamic tissue that possesses interesting mechanical properties as a result of its organic and inorganic composition [1]. Such properties lead to relevant features connected to accomplishing the following functions [2]: allowing locomotion, providing rigid support and places for muscle action, providing a protective shield for the internal organs and bone marrow, acting as ion backup for the maintenance of homeostasis minerals, acting as an endocrine organ that regulates the metabolism [3] and maintains an acid-base balance, and providing a hematopoiesis environment inside of medullar spaces [4]. Macroscopic bone anatomy is composed of cortical and trabecular bone; each one has mechanical properties that follow its histological characteristics. On the one hand, cortical bone has a high density and low porosity—these features endow it with great compressive strength, enabling it to contribute to the mechanical role of bone [5]. It is also stiffer with a low toughness, as compared with other biomaterials and human tissues. Its microscopic pores permit vascular and neural supply, and the delivery of nutrients, but its deterioration rapidly compromises mechanical integrity and the loss of strength during ageing [6]. On the other hand, trabecular or spongy bone has high porosity, with pores making up 50–90% of the total volume—consequently, this reduces its compressive strength but increase its resistance to strain. Likewise, it contributes to providing internal support and increased surface area for red bone marrow, blood vessels and other connective tissues which are in contact and interact with bone [5,6].

Bones are composed of cells; they participate in process like bone growth, modelling and remodeling. The main cells and functions include: osteoblasts, instructed to create and maintain the skeleton architecture [7–9]; osteoclasts, able to remove mineral bone matrix and devoted to dissolving calcium phosphate crystals and digesting collagen, linked to diseases such as arthritis, cancer and osteoporosis, among others, when they develop pathogenic roles [10,11]; and osteocytes, which perform the role of mechanotransduction, the ability to sense mechanical stimuli and translate them into biochemical signals that regulate the action of other cells and communicate with osteoblasts and other associates [12]. These cells, with their self-adaptive abilities, guide bone fate and bone remodeling, the process through which bone undergoes substantial changes in structure, shape, properties and composition according to the mechanical and physiological environment [13]. Bone remodeling is essential in tissue repair, engineering and regeneration approaches, and, being influenced by mechanical cues, it proves urgent to develop and apply reliable biomechanical models in parallel to the development of bone replacements and implants.

The bone remodeling process is essentially the same in cortical and trabecular bone, and its functions include: the replacement of primary bone with secondary bone, which is more mechanically competent; the removal of ischemic or microfractured bone; and the promotion of correct calcium homeostasis [2,14]. This process involves simultaneous resorption and formation, contrary to bone modeling (formation) [15], as result of osteoblasts and osteoclasts action. Both cooperate in the remodeling process in what is called a “basic multicellular unit” (BMU). According to the literature, the remodeling process consists of three phases: resorption, reversal and formation [16]. Bone adaptation to mechanical loading, as one of the causes of the bone remodeling process, is referred to as Wolff’s law or the “law of bone formation”. This law suggests that bone density changes in response to variations in the functional forces of the bone. Therefore, bone atrophy occurs when bones are not mechanically stressed, while hypertrophy appears when they are over-stressed [17].

The specific study of proximal femur biomechanics has led to interesting biomechanical models that have been used for years to design prosthesis for total hip replacement. In 1867, Culmann and von Meyer presented their work to the Society for Natural Science about the internal architecture of the human femoral head and the related stress trajectories. Von Meyer demonstrated arched trabecular patterns in a sagittal femoral section and Culmann suggested that the patterns seemed to be associated with the principal stress produced by functional loading, inspired in a crane that he was designing with a similar shape [18]. In 1870, Wolff developed his “trajectorial theory”, in which he proposed the path that physiological forces seemed to take, notably through the proximal femur, as shown by the trabecular patterns. Wolff emphasized the fact that these columns crossed at right angles [19]. In 1917, Koch investigated femoral mechanics considering femur as an isolated beam structure whose main stresses occurred as a result of the body weight (BW) and did not consider the effect of surrounding muscles. He concluded that BW produces two different sets of stress lines: compressive stresses, along the medial side, and tensile stresses, on the lateral side [20].

Koch’s model has been used for designing stems for total hip replacement. Consequently, the conventional stems use the medial side as a support because that set of lines transfers compressive loads. Some researchers have investigated the applicability of Koch’s model in depth, with interesting conclusions. Rybichi [21] proved, using Koch’s model, that walking produces a force equal to 70% of its fatigue strength; therefore, the risk of fracture of the greater trochanter would be too high. Also, Fetto and Austin [22] used parameters from Koch’s model for predicting the femoral shape, but they found that the computer predicted an unnatural shape of the femur with an expanded diaphyseal diameter. In fact, Koch’s model does not accurately describe the femoral biomechanics because it ignores the muscle action. If taken into account, the forces generated by the iliotibial band and by the vastus lateralis–gluteus medius complex create a tension band effect that converts the tensile stresses of the lateral femoral column into compressive stresses [22,23]. This ascertains that cortical femur bone is undergoing compressive stresses in normal performance, in accordance with its histological characteristics. These differences between models are schematically presented in Figure 1.

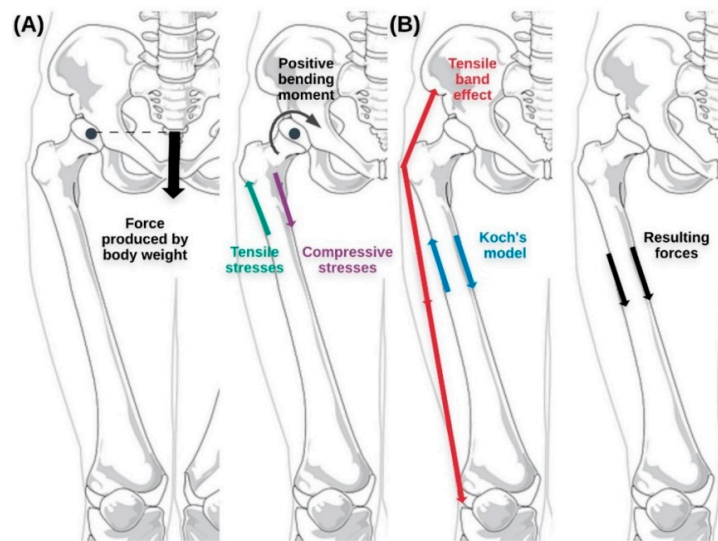


Figure 1. Comparison between: (A) Koch's model that takes into account only the BW effect, and (B) considering the forces that are generated by iliotibial band and the vastus lateralis–gluteus medius complex.

Consequently, the common processes and biomechanical models applied for designing artificial femoral stems should be changed, so as to transfer load, not only in the medial column, but also to the lateral regions. Accordingly, in this study we propose a biomechanical model that considers body weight and muscle action, a model which is helping to develop innovative hip prostheses designs, aimed at improved usability, in accordance with the increasing of physiological and mechanical demands from young and active people.

In this study, we describe the proposed biomechanical model, which also takes into account cortical and trabecular regions and the orthotropic properties of bone. Besides, we apply the model to analyzing different loading cases, linked to daily activities of active patients (sitting down and standing up, walking, jogging, knee bending, walking up and down stairs, among others). The obtained simulation results, which show the stress state of intact bone according to a complete biomechanical model, can be used as a reference. We consider that these results can be employed for analyzing the changes produced by femoral implants on the stress state of healthy bone, and for predicting their potential impact on triggering stress shielding effects, as finally discussed. It is important to highlight that we concentrate on the proximal region, as it is the one suffering from long-term bone resorption in most state-of-the-art implants. A final analysis, in which the effect of an implant on the stress field of normal bone is shown, helps to validate the proposed approach.

2. Materials and Methods

2.1. Geometric Model

For obtaining the human proximal femur, a Digital Imaging and Communications in Medicine (DICOM) file was downloaded from a virtual library, the Cancer Imaging Archive, with the reference TCGA-VP-A878. The images in the DICOM file have a slice thickness of 2 mm on the axial plane and 0.909 mm on the coronal and sagittal planes, being each one 512×512 pixels in size. The DICOM file was imported into 3D Slicer 4.10.2[®] for segmenting the right femur and its cortical bone (Figure 2A), by using threshold, level tracing, paint, erase and smoothing tools. Then, the trabecular bone was obtained by employing logical and Boolean operations (Figure 2B). 3D Slicer[®] permits the export of the segmentation of femur, cortical and trabecular bone as an .stl or .obj file. The stereolithographic or standard tessellation files are imported into Meshmixer[®] to inspect, repair and smooth the meshes. Finally, meshes are introduced into NX 10[®] and further manually processed as solid files.

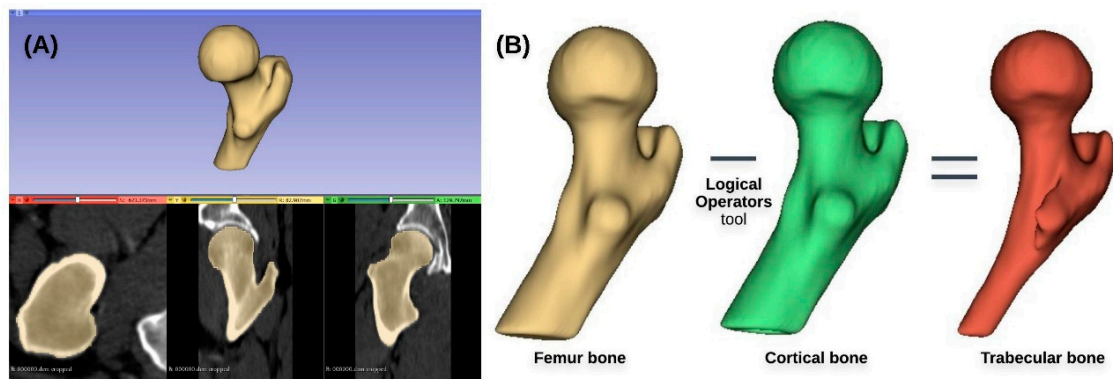


Figure 2. (A) The segmentation of right femur using 3D Slicer®. (B) The process to obtain the trabecular bone using Logical Operators tool.

2.2. Finite Element Model

NX 10® (Siemens PLM Software Solutions, Plano, Texas, US) was used for performing finite element analyses (FEA) employing its Nastran solver. Each bone was meshed using 3D tetrahedral elements (CTETRA 4 and CTETRA 10 elements from NX) with an overall element size of 1.87 mm, which was selected after performing convergence analyses using both the p-method (progressive increase in the higher order of the shape functions used) and the h-method (progressive increase of the number of elements). Accordingly, tests with different element sizes (0.94 mm, 1.45 mm and 1.87 mm) and with different form functions (4-node and 10-node tetrahedral elements) were performed and the differences in results below 2% were verified. Finally, a compromise in terms of calculation speed and quality of results, with 1.87 mm elements and the 10-node tetrahedral elements, was chosen. Cortical bone was meshed with 75,160 elements and 132,598 nodes, while trabecular bone was meshed with 96,815 elements and 145,684 nodes. Both meshes were bonded using gluing surface-to-surface tools and employing a search distance of 0.2 mm. The FEA was developed considering orthotropic properties of bone, according to previous research about its mechanical features. Elastic properties and yield limits of cortical and trabecular bone were estimated using the apparent density ($\text{kg}\cdot\text{m}^{-3}$), which was obtained employing the “Segment Statistics” tool of 3D Slicer® (see Figure 3) and considering its relationship with the Hounsfield units (HU). This relationship was based on the linear relation described by Rho et al. [24]:

$$\rho_{app} = 0.523HU + 1000 \tag{1}$$

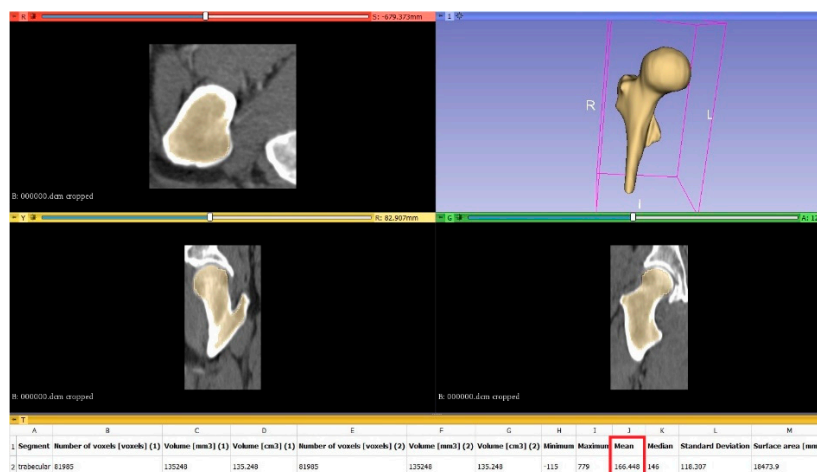


Figure 3. Trabecular bone segment statistics.

Young’s moduli (E_z) and yield limits (σ_z) of cortical and trabecular bone in the longitudinal (compressive) direction, were estimated using the equations described by Keyak et al. [25]:

$$E_z = 14900\rho_{app}^{1.86} \tag{2}$$

$$\sigma_z^C = 102\rho_{app}^{1.8} \tag{3}$$

Furthermore, Young’s modulus and shear modulus in the transverse direction, for both bone types, were estimated using Pithioux’s laws [26]. We considered shear modulus for cortical bone to be the same as for trabecular one:

$$E_x = E_y = 0.6E_z \tag{4}$$

$$G_{yz} = G_{zx} = 0.25E_z \tag{5}$$

Shear modulus in the longitudinal direction was obtained from the experimental equation of Pithioux et al. [27] that relates it to the transverse shear modulus:

$$G_{xy} = 0.7G_{yz} \tag{6}$$

Compressive yield limits in the transverse direction depend of longitudinal compressive limit, as also happens with the tensile and shear limits in i^{th} and j^{th} directions, which are related to the compressive ones by the empiric correlation described by Pithioux [26]:

$$\sigma_x^C = \sigma_y^C = 0.6\sigma_z^C \tag{7}$$

$$\sigma_i^C = 2\sigma_i^T \tag{8}$$

$$\sigma_{ij} = 0.25\sigma_i^C \tag{9}$$

Table 1 summarizes the elastic properties of both bones. The Poisson’s ratios in the longitudinal and transverse directions were obtained from the literature [28]. Table 2 includes the yield limits of cortical bone, which are useful to calculate the Tsai–Wu coefficients, as further analyzed.

Table 1. Material properties of cortical and trabecular bone (Young’s modulus, shear modulus and Poisson’s ratios).

Properties	Cortical Bone	Trabecular Bone
E_x (MPa)	9753.3	3969.8
E_y (MPa)	9753.3	3969.8
E_z (MPa)	16255.6	6616.3
G_{xy} (MPa)	2835.7	2835.7
G_{yz} (MPa)	4063.9	4063.9
G_{zx} (MPa)	4063.9	4063.9
ν_{xy}	0.4	0.4
ν_{yz}	0.25	0.25
ν_{zx}	0.25	0.25

Tsai–Wu criterion, an extension of Hill’s criterion that takes into account the difference in compression and tension behavior of cortical bone [29], is calculated using representative loads for

analyzing fracture risk regions and changes in the biomechanics of proximal cortical femur. The general form for Tsai–Wu criteria for transversely isotropic material is:

$$f(\sigma) = [F_1\sigma_{zz} + F_2(\sigma_{xx} + \sigma_{yy}) + F_{11}\sigma_{zz}^2 + F_{22}(\sigma_{xx}^2 + \sigma_{yy}^2) + F_{66}\tau_{xy}^2 + F_{44}(\tau_{yz}^2 + \tau_{zx}^2) + 2F_{12}(\sigma_{zz}\sigma_{xx} + \sigma_{zz}\sigma_{yy}) + 2F_{23}\sigma_{xx}\sigma_{yy}]^{1/2} \quad (10)$$

where $F_1; F_2; F_{11}; F_{22}; F_{44}; F_{66}$ are coefficients calculated from the yield limits of cortical bone (Table 3) and $F_{12}; F_{23}$ are determined experimentally. In this study, they were considered to be equal to zero. The Tsai–Wu field ($f(\sigma)$) helps to analyze risk regions: those above a value equal to 1.

$$F_1 = 1/\sigma_z^T - 1/\sigma_z^C; F_2 = 1/\sigma_x^T - 1/\sigma_x^C; F_{11} = 1/\sigma_z^T\sigma_z^C; F_{22} = 1/\sigma_x^T\sigma_x^C; F_{44} = 1/\sigma_{zx}^2; F_{66} = 1/\sigma_{xy}^2 \quad (11)$$

Table 2. Yield limits of cortical bone (tensile, compression and shear limits).

Yield Limits (MPa)	Cortical Bone
σ_z^T	35.5
σ_x^T, σ_y^T	21.3
σ_z^C	71.1
σ_x^C, σ_y^C	42.6
σ_{xy}	10.7
σ_{yz}, σ_{zx}	17.8

Table 3. Tsai–Wu coefficients for cortical bone.

Tsai–Wu Coefficients	
F_1 (mm ² /N)	0.0141
F_2 (mm ² /N)	0.0235
F_{11} (mm ⁴ /N ²)	3.96×10^{-4}
F_{22} (mm ⁴ /N ²)	1.1×10^{-3}
F_{44} (mm ⁴ /N ²)	3.168×10^{-3}
F_{66} (mm ⁴ /N ²)	8.8×10^{-3}

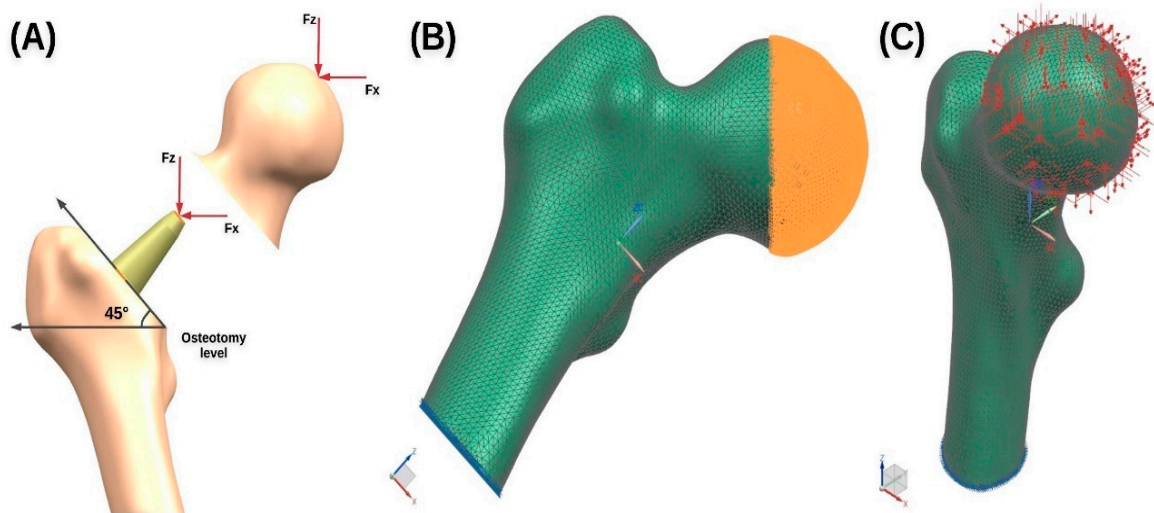
2.3. Boundary Conditions

With the increasing success of hip replacements, the decreasing average age of patients and growing expectations about the implant durability, Bergmann et al. [30] measured the contact forces in the joint, using instrumented stems in ten people during nine of the most physically demanding and frequent activities of daily living. This study is performed considering that pre-clinical strength tests on stems require realistic in vivo loads from younger and more active patients. Likewise, these loads require simplifications to be applicable for simulator tests and numerical analyses [30]. These loads depend of the body weight of each patient. In this study we employ the average weight of Peruvian men (71.3 kg). For obtaining the correct loads (shown in Table 4) a factor is used, which results in dividing the average Peruvian men’s weight by 100 kg, because the data from the reference study were given for that average weight. ISO (International Standardization Organization) force, employed widely to test the stems according to the ISO 7206-4 standard, was also considered.

Table 4. Standardized loads for each of the daily activities considered for the study. * ISO 7206-4.

	Cycling	Sitting Down	Standing Up	Walking	Staying	Stairs Up	Knee Bending	Stairs Down	Jogging	ISO * Force
$-F_x$ (N)	299.5	714.4	1125.1	596.8	681.6	829.9	857	773.6	884.8	-
F_y (N)	-41.4	-62.7	49.9	17.1	-35.7	-48.5	-37.1	-55.6	-15	-
$-F_z$ (N)	805.7	1931.5	2481.2	1931.5	2280.2	2763.6	2054.9	2611	3222	2300

Proximal femur was placed in NX[®] according to the femoral coordinate system [30] and was rotated 45 degrees clockwise around the Y axis for simulating the load transfer that occurs between the hip and femur in the acetabulum (Figure 4B) and considering the accepted neck shaft angle of 135° [31]. This angle was used to cut the femoral neck to insert the stem into the femoral cavity, so it may be possible compare the stress between intact and implanted femur applying the same loads to the stem because it will be in the same position (Figure 4A). This region was composed of 44,772 nodes, upon which the forces were applied (Figure 4C). The flat parts of both bones were fixed.

**Figure 4.** (A) Osteotomy level. (B) Acetabulum region where the load is applied. (C) Boundary conditions.

2.4. Post-Processing

In order to perform results post-processing, the proximal femur was cut longitudinally using a parallel XZ plane, for measuring the maximum principal stress (MPS), a stress indicator that was used in this study according to examples from the literature [32–34]. The MPS was calculated on the medial and lateral sides and simulation results were analyzed accordingly.

The medial side was considered to have three differentiated regions for evaluation purposes: the external cortical (EC), the internal cortical (IC) and the trabecular (T); while the lateral side was considered to have just two representative regions for the evaluation purposes: the internal cortical (IC) and the trabecular (T). In each region of interest, six control points were taken, point 1 being placed at the top of the femur and point 6 at the bottom, as depicted in Figure 5. Control points were used for plotting MPS, as further detailed in the following results and discussion section. Apart from employing the MPS values, the Tsai–Wu field was also obtained and represented for providing additional insight to the discussion of results.

Apart from the presented proximal femur model, a final application case was also incorporated into the discussion and future proposals section to illustrate the potentials of the approach. In the application case, an unconventional prosthetic stem was implanted and simulated. Meshing procedures, bone properties, loads applied, and boundary conditions corresponded to aforementioned explanations.

The implant stem was modeled with titanium alloy and meshes with a similar size to that employed for cortical and trabecular bones. In that final application case, gluing between bone regions and implant was also applied, as contact condition, which would represent the case of a cemented implant. Again, NX 10[®] (Siemens PLM Software Solutions, Plano, Texas, US) was used both for designing the implant and simulating its performance and effects on remaining bone.

This final case was performed to show that the stress field of normal bone is importantly modified by the incorporation of prostheses, and that the results from the FEM analyses upon intact bone can be used for comparing stress fields before and after implantation, and, hence, selecting the most adequate implant geometries and materials.

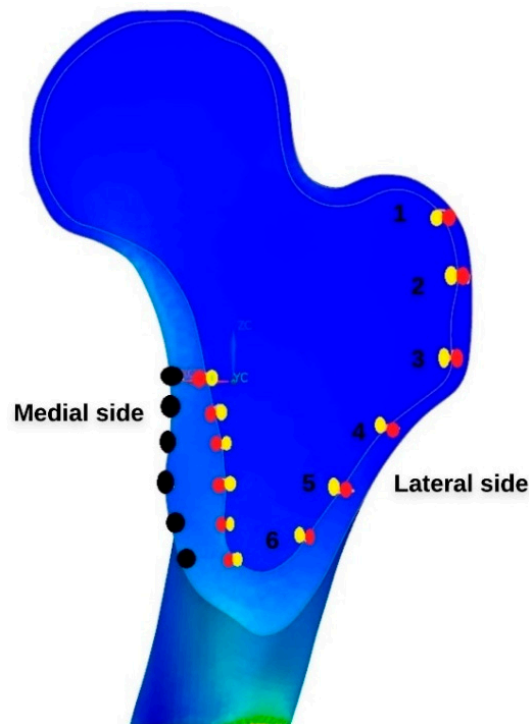


Figure 5. View of the proximal femur with the control points on the medial and lateral side.

3. Results

The simulation results are summarized in the present section. First of all, Figures 6–9 plot the maximum principal stress occurring at the control points when applying the standardized loads for each of the daily activities considered for the study (those summarized in Table 4). The graphs resulting from the different loading conditions are presented in four groups, according to the trend shown. The first group is composed of walking, staying, walking up and down stairs, and jogging (Figure 6); the second group is devoted to standing up and knee bending (Figure 7); the third presents cycling and sitting down (Figure 8); and the fourth is composed of ISO force (Figure 9). Besides, the maximum and minimum stresses are shown in Table 5, and they always appear on the fixed section of each simulation.

Then, for visual purposes and for providing more complete information for direct visual inspection and comparative purposes, a daily activity of each group is selected to show the stress and Tsai–Wu fields of proximal femur. Jogging, standing up, sitting down and ISO force are chosen as representative cases because they led to the highest stress of each group. Figures 10–13 show different views of the stress fields considering a range of -1 to 5 MPa, and Figures 14–17 present the Tsai–Wu fields in a range of 0 to 0.5 .

Table 5. Maximum and minimum principal stresses for different loading conditions.

	Cycling	Sitting Down	Standing Up	Walking	Staying	Stairs Up	Knee Bending	Stairs Down	Jogging	ISO Force
Max. MPS (MPa)	6.09	14.51	27.67	13.96	14.29	17.26	20	15.77	20.25	42
Min. MPS (MPa)	-11.37	-27.82	-46.81	-25.57	-27.87	-33.78	-34.18	-31.27	-37.31	-23.24

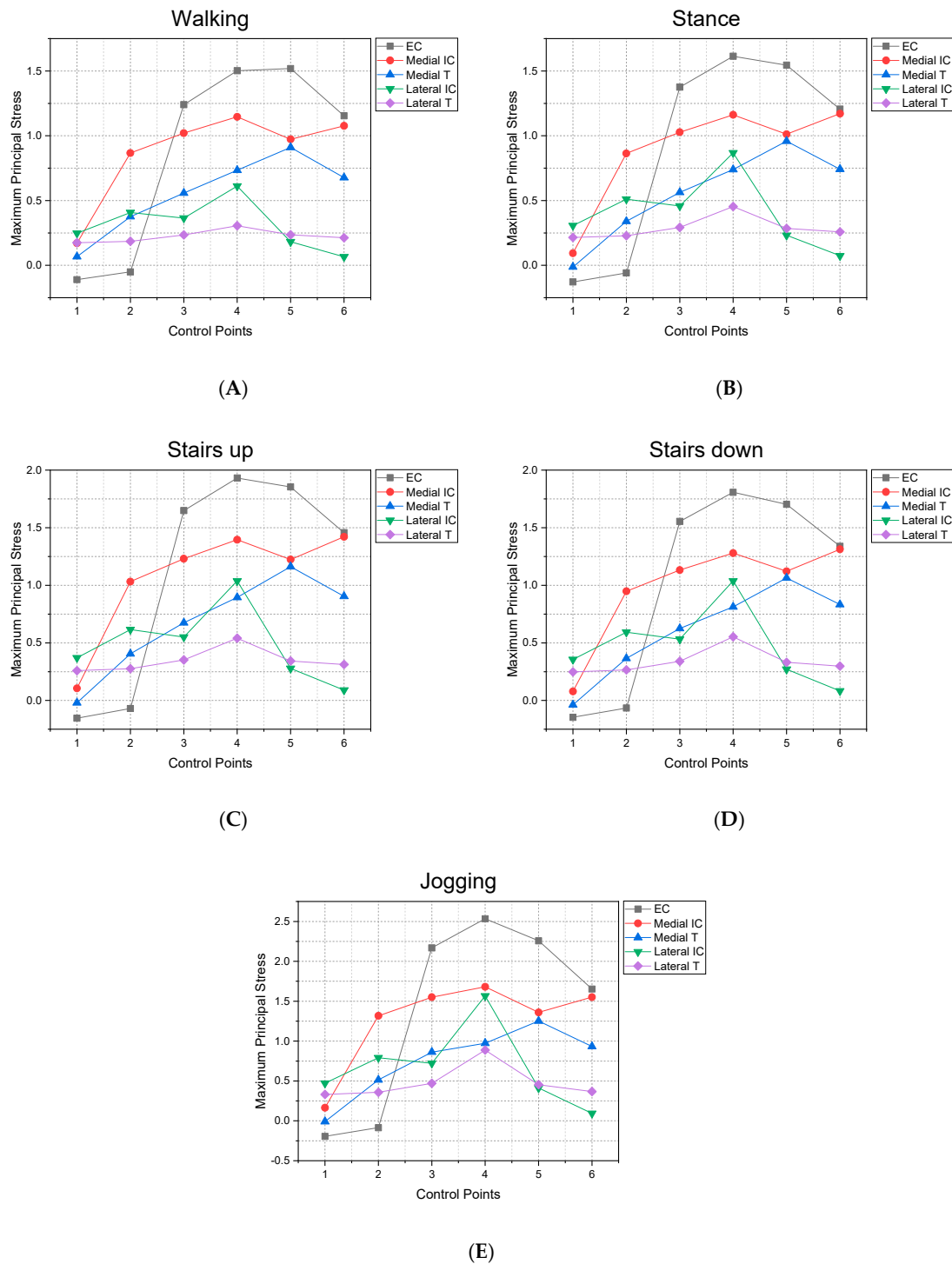


Figure 6. Maximum principal stresses (MPS) occurring at the control points when applying (A) walking, (B) staying, walking up (C) and down (D) stairs and (E) jogging loads.

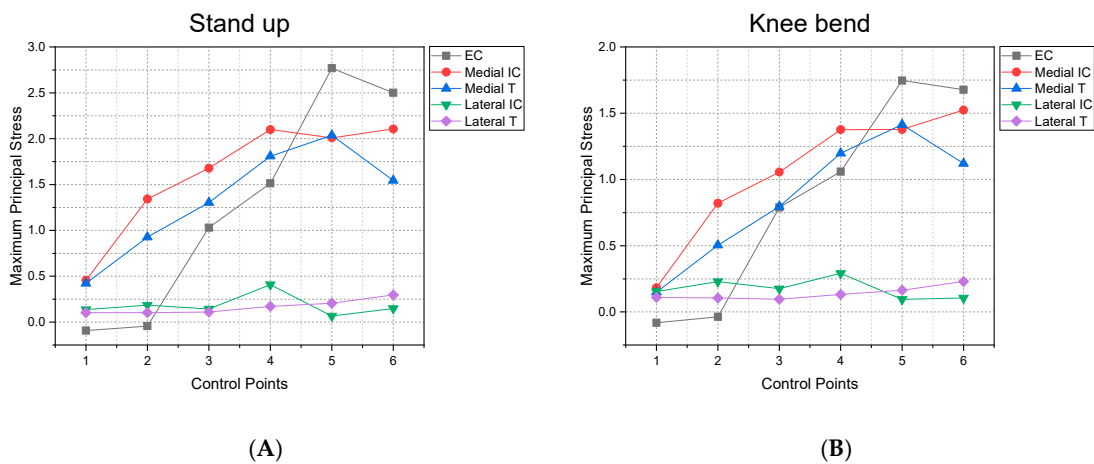


Figure 7. Maximum principal stresses occurring at the control points when applying (A) standing up and (B) knee bending loads.

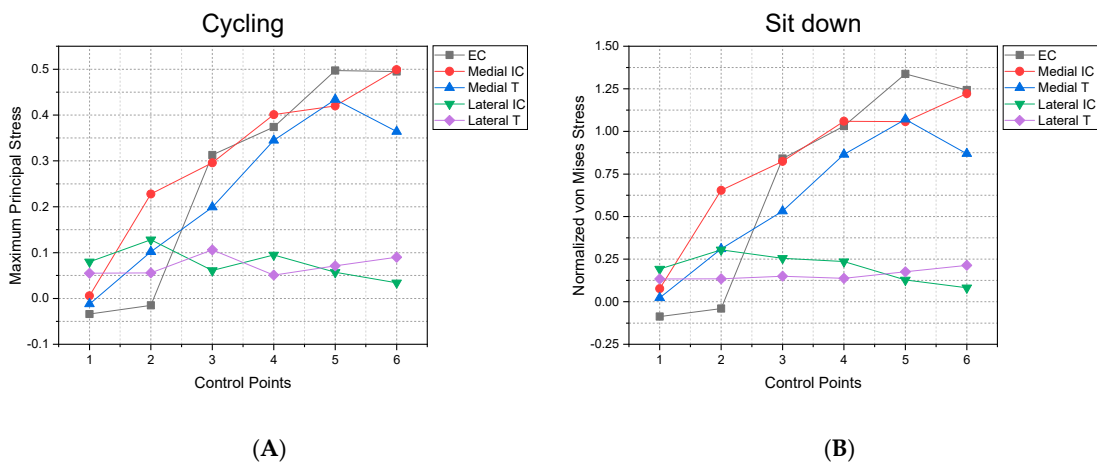


Figure 8. Maximum principal stresses occurring at the control points when applying (A) cycling and (B) sitting-down loads.

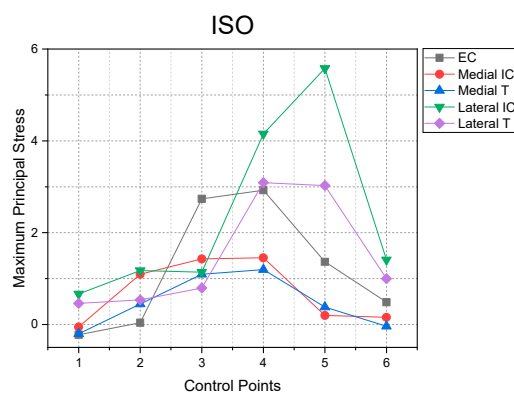


Figure 9. Maximum principal stresses occurring at the control points when applying ISO load.

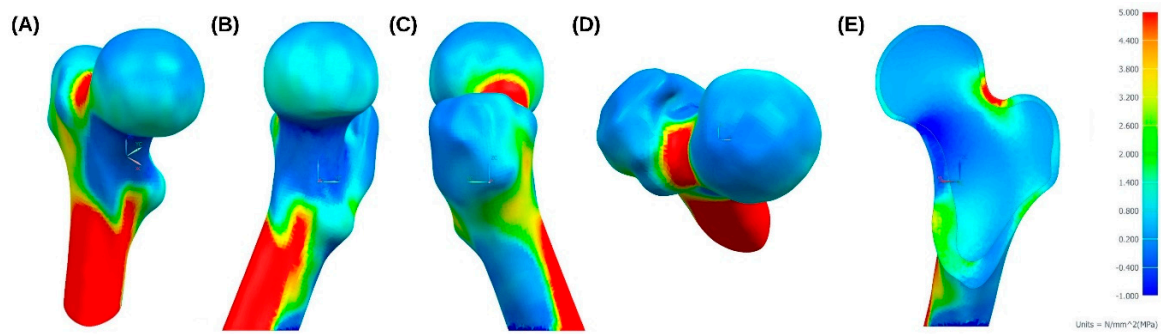


Figure 10. (A) Isometric, (B) right, (C) left, (D) top and (E) back view of maximum principal stress field in proximal femur when applying jogging loads.

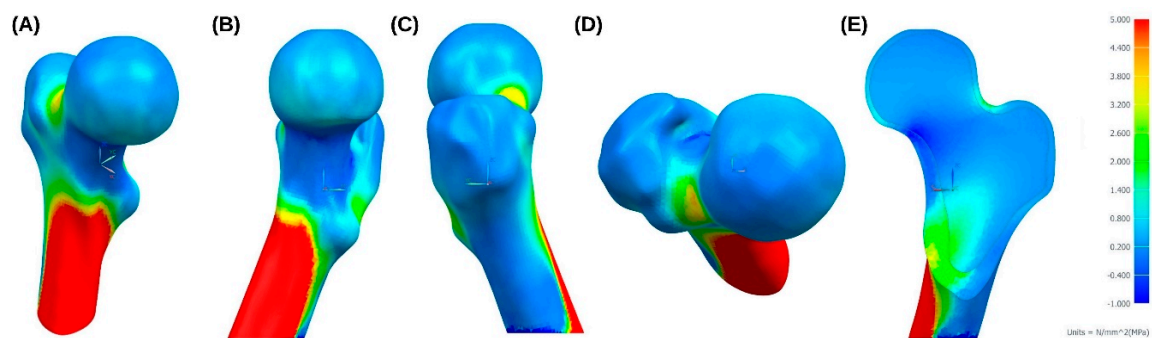


Figure 11. (A) Isometric, (B) right, (C) left, (D) top and (E) back view of maximum principal stress in proximal femur when applying standing-up loads.

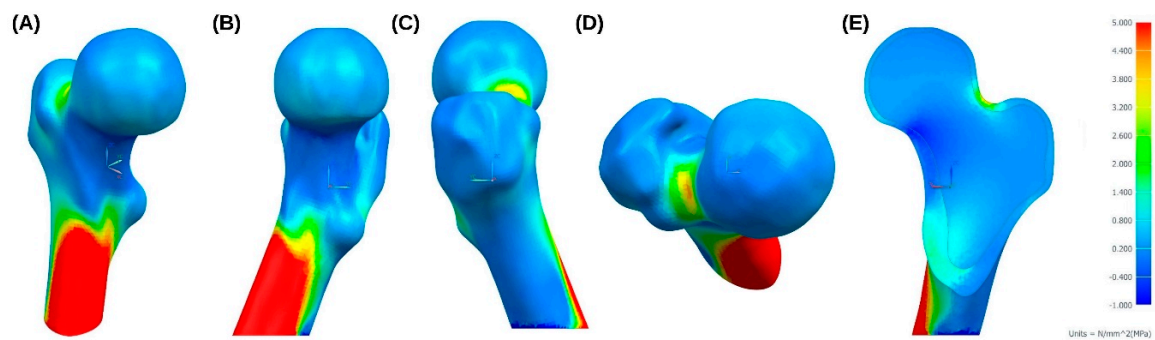


Figure 12. (A) Isometric, (B) right, (C) left, (D) top and (E) back view of maximum principal stress field in proximal femur when applying sitting-down loads.

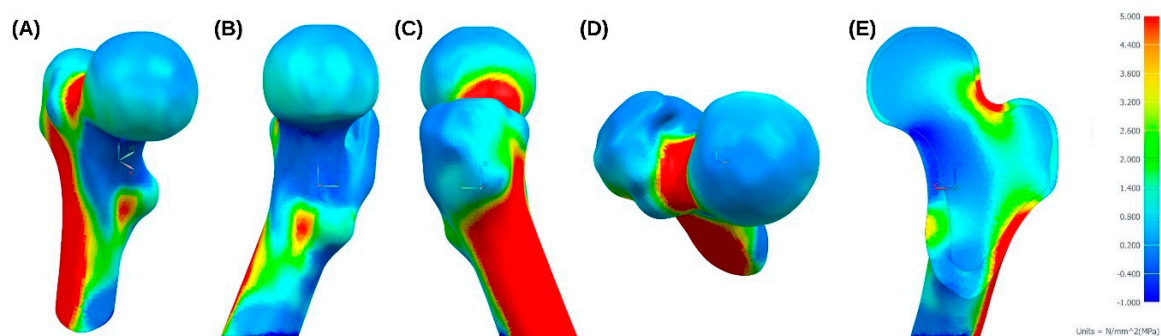


Figure 13. (A) Isometric, (B) right, (C) left, (D) top and (E) back view of maximum principal stress in proximal femur when applying the ISO force.

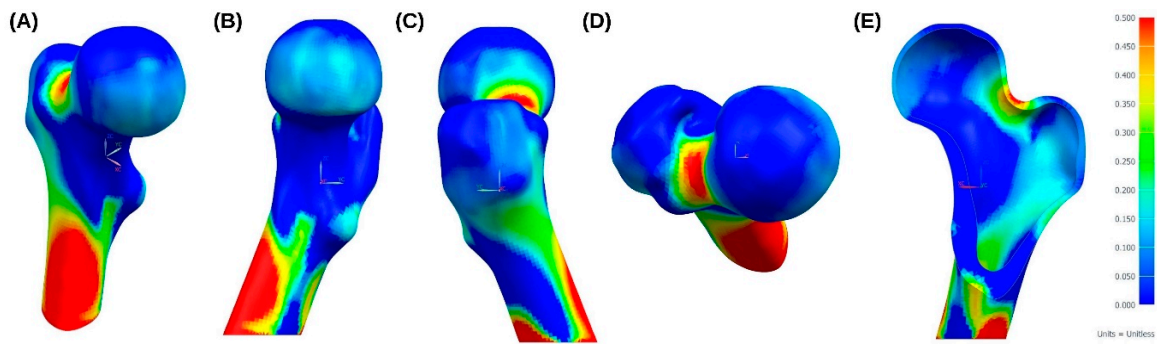


Figure 14. (A) Isometric, (B) right, (C) left, (D) top and (E) back view of Tsai–Wu field in proximal femur when applying jogging loads.

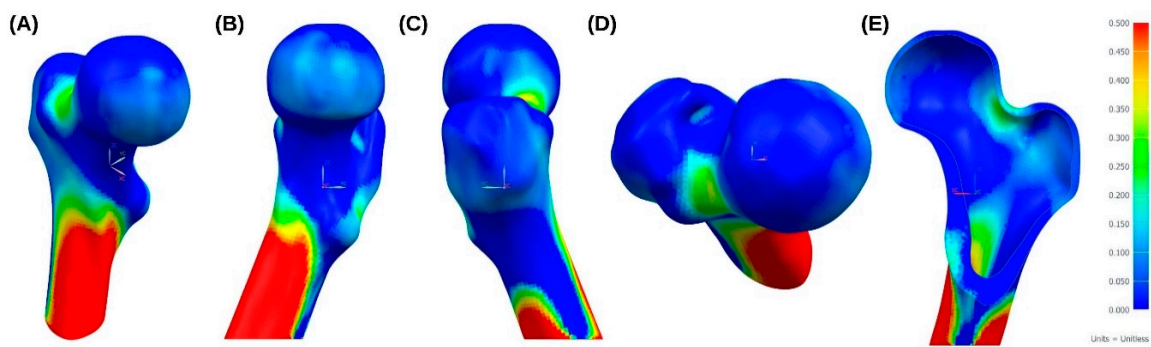


Figure 15. (A) Isometric, (B) right, (C) left, (D) top and (E) back view of Tsai–Wu field in proximal femur when applying standing-up loads.

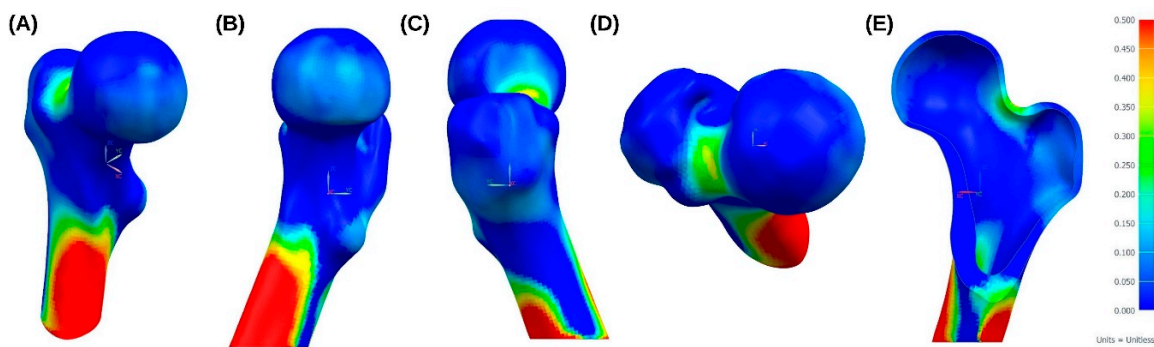


Figure 16. (A) Isometric, (B) right, (C) left, (D) top and (E) back view of Tsai–Wu field in proximal femur when applying sitting-down loads.

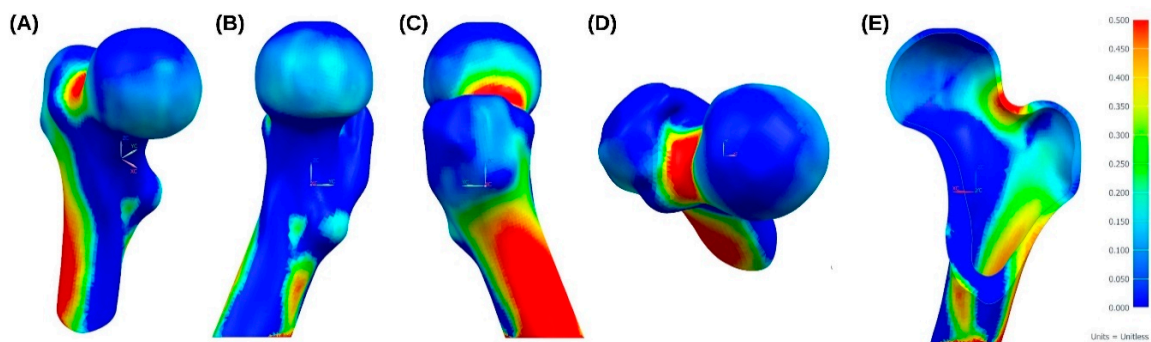


Figure 17. (A) Isometric, (B) right, (C) left, (D) top and (E) back view of Tsai–Wu field in proximal femur when applying the ISO force.

4. Discussion and Future Proposals

The graphs from groups 1, 2 and 3 show higher values for the cortical stresses than for the trabecular ones, which can be explained because cortical bone has a higher Young's modulus and, according to the mechanical concepts, the stiffer material withstands more load. Likewise, global post processing results, which show the stress fields provide similar information. In addition, these graphs show a higher stress level on the medial than on the lateral side, but when both sides are closer to each other the lateral stress tends to increase. Group 4 behaves in the opposite way to the other groups, maintaining higher stress for the cortical bone but with the lateral more loaded than the medial side.

The femoral neck and subtrochanteric region are zones with the most risk of fracture according to the Tsai–Wu field (Figures 14–17); the representative loads that increase the risk of fracture are jogging and ISO force. Tellache et al. [29] used three proximal femurs for testing the femoral strength in one leg position and applying the load on femora heads and concluded that rupture of proximal femur begins in the neck, therefore transcervical neck fracture is one of the causes of hip replacement. The neck plays an important role in the biomechanics of femur because it enables the correct transfer of load from the head to the rest of femur; when femoral neck is removed (Figures 4A and 18) the load transfer changes and this leads to the beginning of stress shielding problems.

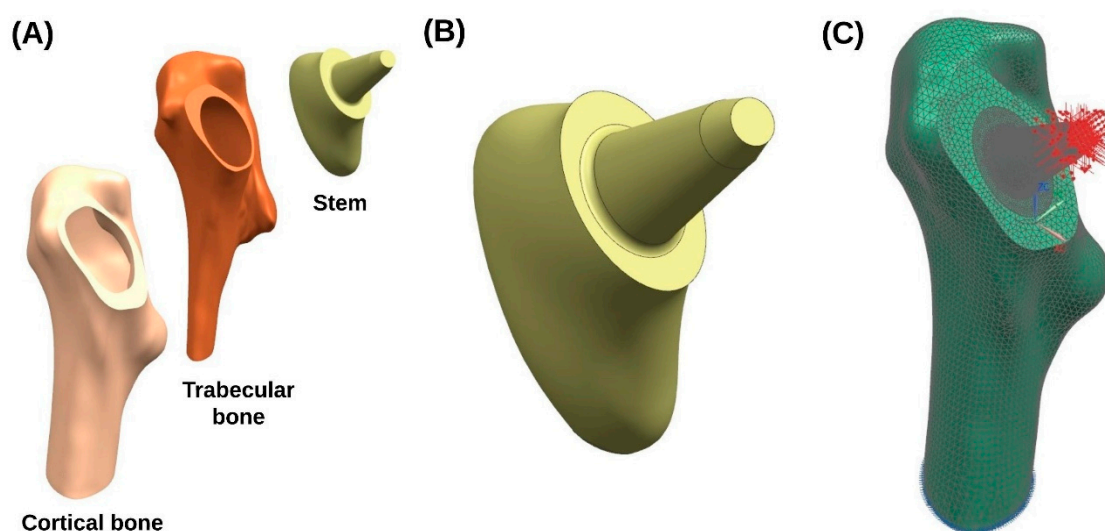


Figure 18. (A) Exploded view of the implanted femur. (B) Short stem. (C) Boundary conditions.

Another aspect promoting stress shielding is connected to differences between the mechanical properties of bone and those from the biomaterials used as substitutes. For instance, the difference between the Young's modulus of Ti-6Al-4V, frequently used to manufacture stems, and bone is responsible for the stress shielding effect common in femoral prostheses. This effect is studied, to advance potential applications of the proposed modeling approach, by introducing a short titanium stem (Figure 18B) into the femoral cavity (Figures 4A and 18A) and simulating intact (Figure 4C) and implanted femur (Figure 18C). Stand up load is chosen as a representative case. The trabecular region is fixed to the cortical one and the implant is fixed to the bone in the implant position. Being common alloys nearly ten times stiffer than bone, their employment importantly modifies the stress field of implanted femurs, with respect to intact ones, as shown in the example of Figure 19, which shows higher stresses in the prosthesis region. The osteotomy level also plays a significant part in the biomechanics of proximal femur, as in some surgeries part of the greater trochanter is cut to correctly fit the stem in spite of importantly modifying the stress fields with respect to those present in intact bones, as consequence of the loose of the iliotibial band. Therefore, we envision that the proposed approach may be also useful for surgical planning tasks towards personalized healthcare and user specific designs of implantable devices.

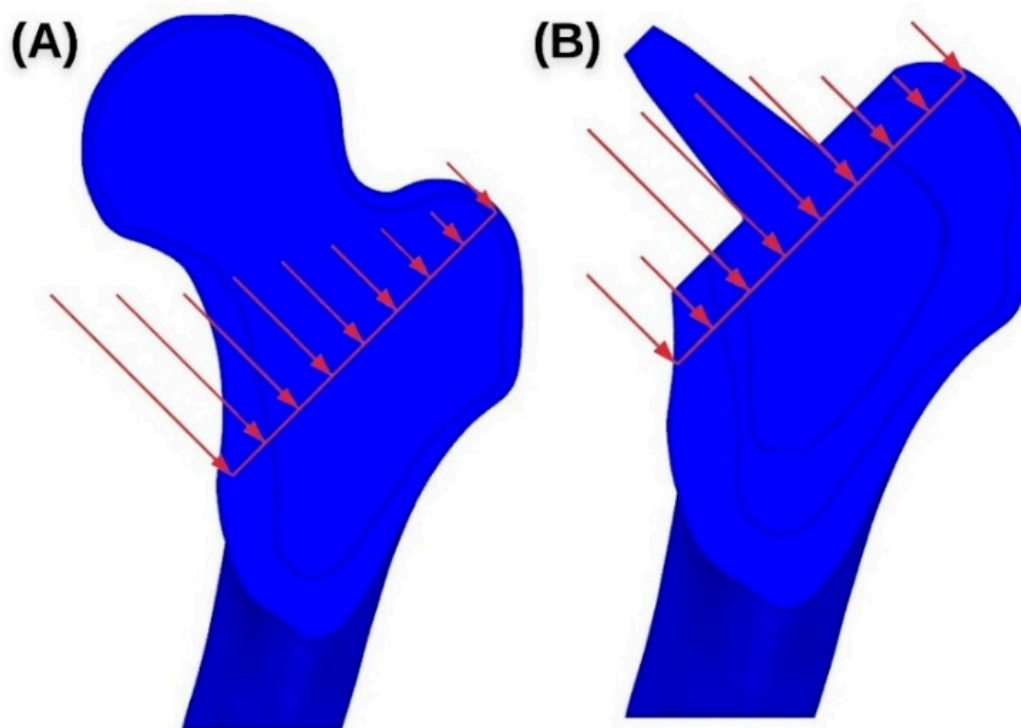


Figure 19. Stress distribution in (A) intact femur and (B) implanted femur. The lengths of the arrows are proportional to maximum principal stresses.

Relative micro-displacements between bone and implant should also be evaluated because they affect the osseointegration process, and, consequently, have an impact in the long-term fixation or secondary stability that reduces aseptic loosening, one of the main causes of stem failure [35].

In the authors' opinion, the biomechanical behavior of stems should be evaluated using different daily activities so as to quantify the potential stress shielding, the difference between intact and implanted femur stresses divided by stress in the intact femur [36], because the aseptic loosening of the implant is influenced by bone resorption and it appears due to stress shielding [37]. Then, comparative studies between designed stems should be performed. The most appropriate for a patient, from a biomechanical point of view, would be the one that leads to a load transfer as similar as possible to the original load transfer in the intact femur.

According to authors' proposal, and using Figures 10–13 as references, it may be possible to qualitatively assess stress shielding by comparing the color maps of intact and implanted femurs and by analyzing whether the ranges are similar, searching for eventual underloaded and overloaded areas. The use of Tsai–Wu fields in order to find the areas more prone to failure is also proposed, so as to prevent periprosthetic fractures.

In fact, distal fixed implants exhibit an adverse bone remodeling with the disappearance of the proximal femur after hip replacement [38], as a consequence of stress shielding problems, especially in the medial side [39]. For that reason, in recent years other kinds of stems, called “short stems”, have been developed as an alternative to the traditional geometries of hip prostheses. Short stems have the following characteristics [40,41]: (a) they help to preserve bone stock, (b) their lateral side is subject to compression forces, (c) they tend to reduce stress shielding and d) they allow for the implantation of conventional stems in revision surgeries. However, short stems may not be the final solution for total hip replacement, considering that their press fit changes the load transfer, as a consequence of the absence of femoral neck, which typically causes underload in the cortical bone region. FEM modeling following a systematic study of daily activities may help to analyze, compare and select between

innovative short-stem designs, which the authors expect to further study in future in vitro and in vivo studies as a complement to the presented computational models and studies.

5. Conclusions

This study has proposed a finite element model considering both cortical and trabecular bone regions, taking account of body weight and muscular loads and using standardized loading cases according to relevant daily activities. The model helps to methodically analyze the state of bones under loading by using relevant control points and stress and Tsai–Wu maps. The maximum principal stress graphs prove useful for assessing changes in the mechanical behavior of the proximal femur and for quantifying stress shielding; also stress maps will be convenient to qualitatively assess stress shielding, which typically appears due to material property mismatches between implants and bones as a consequence of invasive surgical processes or due to prostheses designed without systematically analyzing and optimizing their biomechanical performance. Besides, Tsai–Wu fields help designers to see the areas with the most risk of fracture to prevent periprosthetic fractures, as well as visualize changes in femoral biomechanics.

The authors highlight, as the most interesting cases, the use of jogging, standing-up and sitting-down loads for simulating the implants, as each of these cases is representative from a group of key daily activities, but ISO force is useful for testing epoxy prototypes using their photoelastic properties to confirm the results given by the FEA.

To summarize, the presented analyses help to qualitatively and quantitatively highlight both underloaded regions, which may lead to a loss of bone density in the long term, and overloaded regions, which may lead to hypertrophic regions. As for the future, other aspects with an influence on femoral biomechanics, such as the absence or presence of the femoral neck, stem material or osteotomy level, should be also considered by surgeons and designers in order to achieve a load transfer state after implantation that is as similar as possible to that of the intact femur.

Author Contributions: Conceptualization, methodology and formal analysis, W.S., C.O., A.D.L.; design and simulation, W.S.; writing—original draft, W.S.; writing—review and editing, C.O., A.D.L.; supervision, C.O., A.D.L. All authors have read and agreed to the published version of the manuscript.

Funding: This research was funded by Fondo Nacional de Desarrollo Científico, Tecnológico y de Innovación Tecnológica (FONDECYT) of Peru by contract N°316-2019 that gave the opportunity to W.S. to stay in the Product Development Laboratory at Universidad Politécnica de Madrid for three months.

Acknowledgments: The authors express their gratitude to the Product Development Laboratory at the ETSI Industriales of the Universidad Politécnica de Madrid and to the Mechanical Technology Laboratory at the Mechanical and Electrical Department of the Universidad de Piura. Also, to the members of the División de Ingeniería de Máquinas at Universidad Politécnica de Madrid. The authors acknowledge the support of reviewers and their relevant questions, which led to a more detailed and consistent paper.

Conflicts of Interest: The authors declare no conflict of interest.

References

1. Weiner, S.; Wagner, H.D. The material bone: Structure-mechanical function relations. *Annu. Rev. Mater. Sci.* **1998**, *28*, 271–298. [[CrossRef](#)]
2. Clarke, B. Normal bone anatomy and physiology. *Clin. J. Am. Soc. Nephrol.* **2008**, *3* (Suppl. 3), 131–139. [[CrossRef](#)] [[PubMed](#)]
3. Johannesdottir, F.; Bouxsein, M.L. Bone structure and biomechanics. In *Encyclopedia of Endocrine Diseases*; Elsevier: Amsterdam, The Netherlands, 2018; pp. 19–30.
4. Taichman, R.S. Blood and bone: Two tissues whose fates are intertwined to create the hematopoietic stem-cell niche. *Blood* **2005**, *105*, 2631–2639. [[CrossRef](#)] [[PubMed](#)]
5. Fuchs, R.K.; Thompson, W.R.; Warden, S.J. Bone biology. In *Bone Repair Biomaterials*; Elsevier: Amsterdam, The Netherlands, 2019; pp. 15–52.

6. Hart, N.H.; Nimphius, S.; Rantalainen, T.; Ireland, A.; Siafarikas, A.; Newton, R.U. Mechanical basis of bone strength: Influence of bone material, bone structure and muscle action. *J. Musculoskelet Neuronal Interact.* **2017**, *17*, 114–139. [[PubMed](#)]
7. Florencio-Silva, R.; Sasso, G.R.; Sasso-Cerri, E.; Simões, M.J.; Cerri, P.S. Biology of bone tissue: Structure, function, and factors that influence bone cells. *BioMed Res. Int.* **2015**, *2015*, 1–17. [[CrossRef](#)] [[PubMed](#)]
8. Ferrer Cañabate, J.; Tovar, I.; Martínez, P. Osteoprotegerina y Sistema RANKL/RANK: ¿el futuro del metabolismo óseo? *Anales de Medicina Interna* **2002**, *19*, 5–8. [[CrossRef](#)]
9. Caetano-Lopes, J.; Canhão, H.; Fonseca, J.E. Osteoblasts and bone formation. *Acta Reumatol. Port.* **2007**, *32*, 103–110.
10. Arboleya, L.; Castañeda, S. Osteoclastos: Mucho más que células remodeladoras del hueso. *Rev. Osteoporos. Metab. Miner.* **2014**, *6*, 109–121. [[CrossRef](#)]
11. Bilezikian, J.P.; Raisz, L.G.; Martin, T.J. *Principles of Bone Biology*, 3rd ed.; Academic Press/Elsevier: San Diego, CA, USA, 2008.
12. Bozal, C.B. Osteocytes as mechanosensors in bone. *Actual. Osteol.* **2013**, *9*, 176–193.
13. Doblaré, M.; García, J.M.; Gómez, M.J. Modelling bone tissue fracture and healing: A review. *Eng. Fract. Mech.* **2004**, *71*, 1809–1840. [[CrossRef](#)]
14. Rucci, N. Molecular biology of bone remodelling. *Clin. Cases Miner. Bone Metab.* **2008**, *5*, 49–56. [[PubMed](#)]
15. Boyce, B.F.; Xing, L. Functions of RANKL/RANK/OPG in bone modeling and remodeling. *Arch. Biochem. Biophys.* **2008**, *473*, 139–146. [[CrossRef](#)] [[PubMed](#)]
16. Hadjidakis, D.J.; Androulakis, I.I. Bone remodeling. *Ann. N. Y. Acad. Sci.* **2006**, *1092*, 385–396. [[CrossRef](#)] [[PubMed](#)]
17. Wolff, J. *Das Gesetz der Transformation der Knochen*; Pro Business: Berlin/Heidelberg, Germany, 2010.
18. Skedros, J.G.; Brand, R.A. Biographical sketch: Georg hermann von meyer (1815–1892). *Clin. Orthop. Relat. Res.* **2011**, *469*, 3072–3076. [[CrossRef](#)]
19. Hammer, A. The paradox of wolff's theories. *Ir. J. Med. Sci.* **2015**, *184*, 13–22. [[CrossRef](#)]
20. Koch, J.C. The laws of bone architecture. *Am. J. Anat.* **1917**, *21*, 177–298. [[CrossRef](#)]
21. Rybicki, E.F.; Simonen, F.A.; Weis, E.B. On the mathematical analysis of stress in the human femur. *J. Biomech.* **1972**, *5*, 203–215. [[CrossRef](#)]
22. Fetto, J.F.; Bettinger, P.; Austin, K. Reexamination of hip biomechanics during unilateral stance. *Am. J. Orthop.* **1995**, *24*, 605–612.
23. Santori, N.; Lucidi, M.; Santori, F.S. Proximal load transfer with a stemless uncemented femoral implant. *J. Orthopaed. Traumatol.* **2006**, *7*, 154–160. [[CrossRef](#)]
24. Rho, J.Y.; Hobatho, M.C.; Ashman, R.B. Relations of mechanical properties to density and CT numbers in human bone. *Med. Eng. Phys.* **1995**, *17*, 347–355. [[CrossRef](#)]
25. Keyak, J.H.; Kaneko, T.S.; Tehranzadeh, J.; Skinner, H.B. Predicting proximal femoral strength using structural engineering models. *Clin. Orthop. Relat. Res.* **2005**, *437*, 219–228. [[CrossRef](#)] [[PubMed](#)]
26. Pithioux, M. *Lois de Comportement et Modèles de Rupture des os Longs en Accidentologie*. Ph.D. Thesis, Université de la Méditerranée, Marseille, France, 2000.
27. Pithioux, M.; Lasaygues, P.; Chabrand, P. An Alternative ultrasonic method for measuring the elastic properties of cortical bone. *J. Biomech.* **2002**, *35*, 961–968. [[CrossRef](#)]
28. Peng, L.; Bai, J.; Zeng, X.; Zhou, Y. Comparison of isotropic and orthotropic material property assignments on femoral finite element models under two loading conditions. *Med. Eng. Phys.* **2006**, *28*, 227–233. [[CrossRef](#)] [[PubMed](#)]
29. Tellache, M.; Pithioux, M.; Chabrand, P.; Hochard, C. Femoral neck fracture prediction by anisotropic yield criteria. *Eur. J. Comput. Mech.* **2009**, *18*, 33–41. [[CrossRef](#)]
30. Bergmann, G.; Bender, A.; Dymke, J.; Duda, G.; Damm, P. Standardized loads acting in hip implants. *PLoS ONE* **2016**, *11*, 1–23. [[CrossRef](#)] [[PubMed](#)]
31. Gilligan, I.; Chandraphak, S.; Mahakkanukrauh, P. Femoral neck-shaft angle in humans: Variation relating to climate, clothing, lifestyle, sex, age and side. *J. Anat.* **2013**, *223*, 133–151. [[CrossRef](#)]
32. Mu Jung, J.; Sang Kim, C. Analysis of stress distribution around total hip stems custom-designed for the standardized Asian femur configuration. *Biotechnol. Biotechnol. Equip.* **2014**, *28*, 525–532. [[CrossRef](#)]
33. Rabbani, M.; Saidpour, H. stress analysis of a total hip replacement subjected to realistic loading conditions. *J. Robot. Mech. Eng. Res.* **2015**, *1*, 18–23.

34. Schileo, E.; Taddei, F.; Cristofolini, L.; Viceconti, M. Subject-specific finite element models implementing a maximum principal strain criterion are able to estimate failure risk and fracture location on human femurs tested in vitro. *J. Biomech.* **2008**, *41*, 356–367. [[CrossRef](#)]
35. Ojeda, C. Estudio de la Influencia de Estabilidad Primaria en el Diseño de Vástagos de Prótesis Femorales Personalizadas: Aplicación a Paciente Específico. Ph.D. Thesis, Universidad Politécnica de Madrid, Madrid, Spain, 2009.
36. Cheruvu, B.; Venkatarayappa, I.; Goswami, T. Stress shielding in cemented hip implants assessed from computed tomography. *Biomed. J. Sci. Tech. Res.* **2019**, *18*, 13637–13641.
37. Gargiulo, P.; Gislason, M.K.; Edmunds, K.J.; Pitocchi, J.; Carraro, U.; Esposito, L.; Fraldi, M.; Bifulco, P.; Cesarelli, M.; Jónsson, H. CT-based bone and muscle assessment in normal and pathological conditions. In *Encyclopedia of Biomedical Engineering*; Elsevier: Amsterdam, The Netherlands, 2019; pp. 119–134.
38. Yao, Z.; Lin, T.-H.; Pajarinen, J.; Sato, T.; Goodman, S. Host response to orthopedic implants (metals and plastics). In *Host Response to Biomaterials*; Elsevier: Amsterdam, The Netherlands, 2015; pp. 315–373.
39. Cooper, R.R. The Scientific Basis of Joint Replacement. *JAMA* **1977**, *238*, 2731. [[CrossRef](#)]
40. Morales de Cano, J.; Vergara, P.; Valero, J.; Clos, R. Utilización de los vástagos metafisarios «Próxima» DePuy: Nuestra experiencia a más de cinco años. *Acta Ortopédica Mexicana* **2018**, *32*, 88–92. [[PubMed](#)]
41. Shin, Y.-S.; Suh, D.-H.; Park, J.-H.; Kim, J.-L.; Han, S.-B. Comparison of specific femoral short stems and conventional-length stems in primary cementless total hip arthroplasty. *Orthopedics* **2016**, *39*, 311–317. [[CrossRef](#)] [[PubMed](#)]



© 2020 by the authors. Licensee MDPI, Basel, Switzerland. This article is an open access article distributed under the terms and conditions of the Creative Commons Attribution (CC BY) license (<http://creativecommons.org/licenses/by/4.0/>).